# Accepted Manuscript

Investigation with β-particles and protons of buried graphite pillars in single-crystal CVD diamond

M. Girolami, G. Conte, D.M. Trucchi, A. Bellucci, P. Oliva, T. Kononenko, A. Khomich, A. Bolshakov, V. Ralchenko, V. Konov, N. Skukan, M. Jakšić, I. Sudić, W. Kada, S. Salvatori
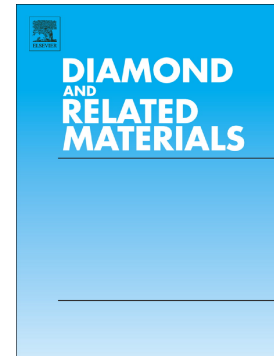
Please cite this article as: M. Girolami, G. Conte, D.M. Trucchi, A. Bellucci, P. Oliva, T. Kononenko, A. Khomich, A. Bolshakov, V. Ralchenko, V. Konov, N. Skukan, M. Jakšić, I. Sudić, W. Kada, S. Salvatori , Investigation with β-particles and protons of buried graphite pillars in single-crystal CVD diamond. The address for the corresponding author was captured as affiliation for all authors. Please check if appropriate. Diamat(2017), doi:10.1016/j.diamond.2018.02.014

# Investigation with *β*-particles and protons of buried graphite pillars in single-crystal CVD diamond

**M. Girolami**[a,*]**, G. Conte**[a,b]**, D. M. Trucchi**[a]**, A. Bellucci**[a]**, P. Oliva**[c]**, T. Kononenko**[d]**, A. Khomich**[d]**, A. Bolshakov**[d,e]**, V. Ralchenko**[d,e,f]**, V. Konov**[d,f]**, N. Skukan**[g]**, M. Jakšić**[g]**, I. Sudić**[g]**, W. Kada**[h]**, S. Salvatori**[c]

[a] *CNR-ISM, Consiglio Nazionale delle Ricerche, Istituto di Struttura della Materia, Sede secondaria di Montelibretti, Via Salaria km 29,300 – 00015 Monterotondo Stazione, Roma, Italy*

[b]*Università degli Studi Roma Tre and INFN, Via della Vasca Navale 84 – 00146 Roma, Italy*

[c]*Università degli Studi Niccolò Cusano, Via Don Carlo Gnocchi 3 – 00166 Roma, Italy*

[d]*A.M. Prokhorov General Physics Institute, Russian Academy of Sciences, 38 Vavilova Str – 119991 Moscow, Russia*

[e]*Harbin Institute of Technology, 92 Xidazhi Str. – 150001 Harbin, P.R. China*

[f]*National Research Nuclear University "MEPhI", Kashirskoye Shosse 31 – 115409 Moscow, Russia*

[g]*Ruder Bošković Institute, Bijenička Cesta 54 – 10000 Zagreb, Croatia*

[h]*Division of Electronics and Informatics, Faculty of Science and Technology, Gunma University, Kiryu, Gunma 376-8515, Japan*

*corresponding author (marco.girolami@ism.cnr.it, +39 06 90672237)

Abstract

*A detailed characterization under $^{90}$Sr β-particles and 4.5 MeV protons micro-beam of a single-crystal CVD diamond-based three-dimensional detector with surface and buried graphite electrodes is presented. Pillar contacts, 300 μm long and 30 μm diameter, were fabricated by using a femtosecond laser operating at 1030 nm wavelength and 400 fs pulse duration. Charge collected under $^{90}$Sr β-particles was measured in front and back irradiation conditions, pointing out that the pillars contribute to the charge collection. Charge collection efficiency (CCE) was measured to be up to 94% under proton beam irradiation. Results of a comprehensive study, including crossed-polarizers imaging, numerical simulation of the electric field distribution, and proton mapping, show that CCE is not affected from the stress induced by the pillar fabrication, and that the electric field strength is high enough to partially compensate for carrier recombination in the defected regions surrounding the pillars.*

Keywords**:** graphite pillars; 3D detectors; single-crystal CVD diamond; *β*-particles; protons.

## 1. Introduction

Three-dimensional (3D) diamond detectors have been recently proposed as an additional technology for the innermost tracking detectors in ATLAS and CMS experiments at CERN [1]. Also, 3D electrode geometries have raised interest in several application fields [2–4], ranging from solar energy conversion to medical imaging. Using the same architecture proposed for silicon and GaAs based devices [5], 3D diamond detectors would indeed show superior performance due to the outstanding radiation hardness and the extremely high resistivity of bulk diamond. Moreover, the low dielectric permittivity of diamond guarantees a relatively lower noise level referred to the input of the front-end electronics.

3D diamond detectors have been recently studied by few groups [6–8], exploiting the local conversion of bulk diamond into graphite by ultrafast (from ns to fs) pulsed laser irradiation. One of the first examples of laser treatment used for the fabrication of buried graphite contacts can be attributed to Walker et al. [9], who created vertical electrodes into the bulk of a natural diamond to reach and connect a conductive buried layer previously fabricated by boron ion implantation. Nowadays, research efforts [10-16] are mainly focused on the optimization of the laser processing parameters, aimed at 1) reducing the graphite column resistivity, 2) enhancing the pillar aspect ratio (length over diameter), 3) improving the buried-contact geometry, and 4) increasing the pillar density. The key requirement is the long-term stability of diamond detectors in terms of charge collection efficiency (CCE), especially under extreme irradiation conditions (high fluences) [17]. Very recently, by using a Ti-Sapphire femtosecond laser operating at 800 nm and 100 fs pulse duration, G.T. Forcolin et al. [18] reported a study about the effect of laser fluence on the pillar properties. Results pointed out a linear dependence of the pillar diameter on the laser beam fluence in the 2–5 J cm$^{-2}$ range, and a strong influence of the laser processing parameters on the stress induced in the bulk diamond, but only a minor effect was observed on the graphite column resistivity. For the first time, they also performed tests with photon and proton micro-beams using Ion Beam Induced Charge (IBIC) and Time Resolved Ion Beam Induced Current (TRIBIC) analysis, highlighting a complete charge collection within the explored active regions of the detector. On the same topic, M.J. Booth et al. [19] reported a more complete IBIC and TRIBIC analysis. They were able to evidence a full charge collection for different geometries of 3D pillars, whereas small differences, depending on the buried-contact geometry, were found in charge sharing among neighboring cells. S. Murphy *et al.* [20] were able to decrease both the dimensions and the resistance of the electrodes by using a spatial light modulator to correct the aberration of the laser beam and the local stress induced by the laser treatment.

Their results showed a resistivity decrease from 2.5 $\Omega$ cm to 0.2 $\Omega$ cm, combined to a lower diamond-on-graphite ratio and to a lower degree of stress induced by graphitic electrodes formation.

In this paper, a comprehensive study of graphite pillars buried in single-crystal CVD diamond fabricated by local graphitization using an ultrafast IR laser is reported. Unlike the 3D structures reported in Refs. 1-7, pillars were not fabricated as "pass-through" columns, but the end of the pillar is located about 100 μm away from the bottom surface, which is therefore completely insulating: this could represent a simple way for the implementation of a 3D stacked detector for particle tracking with no risk for short-circuits between the single layers. Aimed at verifying the effectiveness of pillars in collecting the photogenerated charge, a detailed investigation with beta particles emitted by a $^{90}$Sr source was performed by irradiating the detector from both the top and bottom surface of the sample. Also, aimed at evaluating the presence of lattice defects and stress induced by the laser treatment in the volume surrounding the pillars, and how they can affect charge collection efficiency, IBIC mapping with a 4.5 MeV protons micro-beam was used, in conjunction with Raman analysis and cross-polarized optical microscopy analysis. Moreover, numerical simulations were performed to estimate the electric field distribution within the detector active volume.

## 2. Experimental

### 2.1. Material

A customized "detector-grade" single-crystal (100)-oriented CVD-diamond plate by Element Six [21], 4×4 mm$^2$ large and 0.4 mm thick (with nitrogen and boron impurities content lower than 10 ppb and 1 ppb, respectively), was used for the fabrication of the detector. The four lateral 4×0.4 mm$^2$ faces were polished by using standard mechanical procedures, allowing for a real-time inspection during the subsequent graphitization laser-processing for the realization of the buried contacts. Then, in order to remove any metal and organic residuals, the sample was dipped in hot sulpho-chromic acid solution ($K_2Cr_2O_7$, 1.6% weight, in $H_2SO_4$; 15 min at 120$^o$C), followed by rinsing in *aqua regia* (25% vol. $HNO_3$ in mixture $HNO_3$+HCl; 10 min at 90$^o$C), hot deionized water (1 min at 80$^o$C), and isopropanol (1 min at 25$^o$C).

## 2.2 Detector fabrication

A computer controlled 3-axis stage was used to control the diamond position and translation with respect to the laser focal plane. Local graphitization was performed with a VaryDisk50 pulsed laser (Dausinger + Giesen GmbH), operating at 1030 nm wavelength, repetition rate of 200 kHz and 400 fs of pulse duration. First, the laser beam was focused by an aspheric lens (11 mm focal length) on the back diamond surface: fourteen parallel graphite strips (1.5 mm long, 50 μm wide, 10 μm thick, and 250 μm apart), were drawn at the surface by means of a multi-pass beam scanning technique at a speed of 50 μm/s and a fixed pulse energy of 0.8 μJ (fig. 1a). Fabrication details of the graphite surface contacts, as well as of their electrical characterization, can be found elsewhere [22, 23]. Subsequently, six buried graphite pillars were grown on each surface strip (fig. 1b) at the same pulse energy, moving the sample away from the lens along the laser beam axis. Each pillar was written in a single scanning step at a relative laser focal point/sample speed of 0.5 μm/s. The fabricated array of buried graphite pillars has a body-centered rectangular structure. The 'elementary cell' has lateral dimensions $x = 250 \pm 10$ μm, and $y = 500 \pm 10$ μm. The effective distance between the central pillar and the neighboring ones is 279.5 μm.
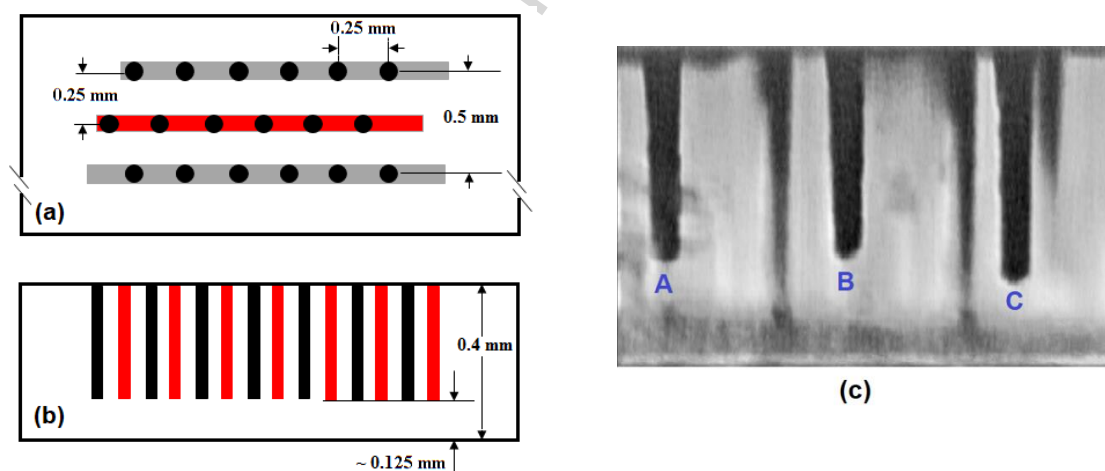


**Fig. 1**. Schematic layout of the 3D detector: a) front view of part of the surface strips connecting buried columns; b) cross-sectional lateral view of the graphite pillars. c) optical microscopy image (taken from the lateral surface of the sample) of a group of three pillars belonging to the same strip.

Fig. 1c shows an optical microscopy image of a group of three pillars belonging to the same strip. As can be seen, the length of the pillars is not equal (pillars A, B and C are 270, 265, and 300 μm long, respectively); after the inspection of a group of 24 pillar, average length was estimated to be $275 \pm 30$ μm. Therefore, the distance between the end section of the pillars and the back surface varies in the range 95 – 155 μm (125 μm on average).

Conversely, the diameter is the same for all the pillars (30 μm), always increasing up to 50 μm near the surface strips.

Cyan-acrylic single component liquid glue was used to fix the device to a single-face Printed Circuit Board (PCB), with copper traces specifically designed for optimizing the connection to the front-end electronics used for detector biasing and signal acquisition. The presence of a hole in the PCB allowed for irradiation also on the back side of the detector. Odd graphite strips (red in fig. 1a) were wire-bonded to a PCB read-out pad (channel 1) by using Al (99%)/Si (1%) 25-μm thick wires. Even strips (grey in fig. 1a), were wire-bonded to a second read-out pad (channel 2). In this way, measurements can be performed either in single-ended (grounded) or differential (floating contacts) mode.
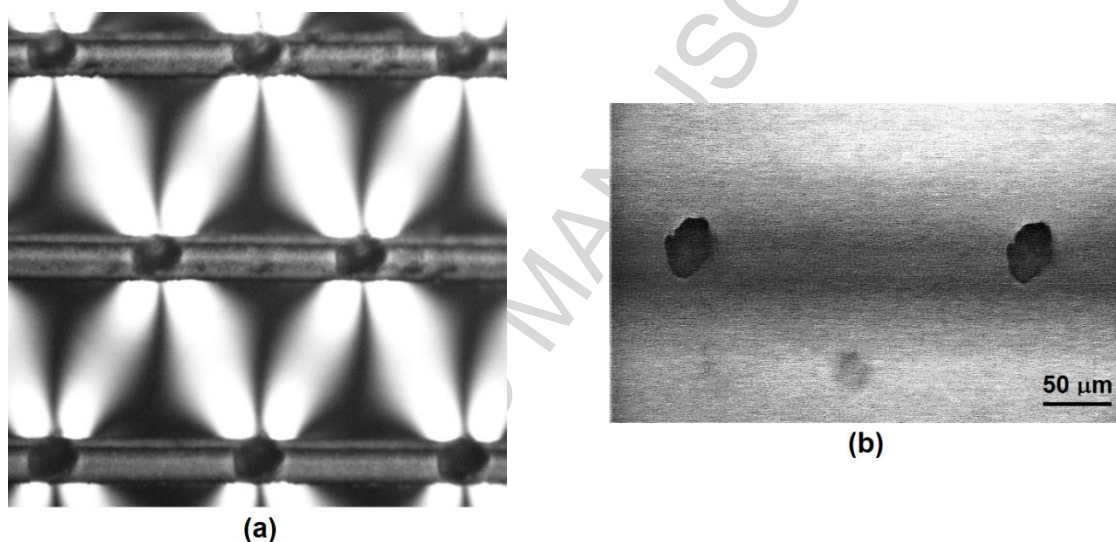


**Fig. 2**. a) Cross-polarized optical microscopy image of a region involving two rectangular cells. The picture shows one central even graphite strip included between two odd ones. b) Optical microscopy image (taken from the back side of the sample) of the end section of two adjacent pillars belonging to the same strip.

Possible stress induced on the virgin diamond plate by the laser treatment was inferred by using crossed polarized optical microscopy. Stressed regions may indeed induce electronic active defects for the charge carrier recombination or trapping, resulting in detrimental polarization effects and affecting severely the charge collection efficiency. Fig. 2a reports the picture of a region between three strips involving two rectangular cells. The buried pillars (black round dots) and the graphite strips on the surface are clearly evidenced. Stressed (white) regions, about 80 – 100 μm long, departing from each pillar and oriented toward neighboring pillars, are also clearly visible. It's worth noting the superposition of some of such "plumes" with others produced in the neighboring cells, whereas a lower stressed region

can be seen between two adjacent pillars belonging to the same strip. Raman analysis, performed in the region within the pillars, evidenced an upshift $(\nu_R - \nu_{R0})$ of about ~2.5 cm$^{-1}$ for the diamond peak position $\nu_R$ from the reference value $\nu_{R0} = 1332.5$ cm$^{-1}$ known for unstrained diamond. This upshift corresponds to a compressive stress $\sigma \approx 1.0$ GPa, as estimated by using the relationship $\sigma = 0.38 \, (\nu_R - \nu_{R0})$ GPa [24]. However, despite the stress, no visible cracks (or other extended defects) are present in the diamond bulk surrounding the pillars, as highlighted in fig. 2b, which shows the end section of two adjacent pillars belonging to the same strip (and having the same length). This suggests that the defects unavoidably introduced by laser treatment at the diamond-graphite interface are mostly point defects in our case, or otherwise defects which cannot be easily detected by optical inspection.

## 2.3. Measurement setup with $^{90}Sr$ source

Experiments with electrons emitted from a $^{90}$Sr $\beta$-source (activity 1 MBq, 1 mm diameter and 1 cm long, QSA Global, code SIFB13505, item 22/2006), were carried out in self-triggering mode, regulated on a selectable amplitude level of the same acquired pulses. The $^{90}$Sr $\beta$-source emits relatively low-energy electrons by $^{90}$Sr to $^{90}$Y decay, with an end-point energy of 0.546 MeV. Then, a second high-energy $\beta$-decay to $^{90}$Zr is observed, with a 2.280 MeV end-point energy. The source holder, a 25 mm long brass cylinder with an aperture of 0.4 mm diameter and a depth of 5 mm, was used both to host the source and collimate the electron emission. The source was maintained 1 cm above the sample surface, thus irradiating the whole detector area. Low-noise and fast rise time CAEN A1422H-F2 (gain 45 mV/MeV in Si) hybrid charge sensitive amplifier with an input test for calibration (C = 1 pF) was used as a first stage for charge signal conditioning. Amplified output signal was analyzed by using a CAEN N6724A 2-channel digitizer (14 bit, 100 MSample/s and 500 mV$_{pp}$ of dynamic range), whereas a CAEN N1471A voltage supply was used for detector biasing. Signal processing was performed by means of a CAEN DPP-PHA Digital Pulse Processor for Pulse Height Analysis. Being the Gaussian pedestal noise evaluated to be equal to 0.18 fC (1100 electrons), the trigger threshold was set to 1500 electrons (corresponding to 0.24 fC). An Agilent 33250A waveform generator, with arbitrary curve capability, was used to produce a calibration signal in order to convert the Pulse Height Distribution (PHD) of the acquired signal (expressed as ADC channels) into femtocoulomb units of the collected charge. The calibration uncertainty is mainly related to the pulse generator accuracy (1%), whereas the non-linearities related to the charge preamplifier and the ADC do not significantly influence the uncertainty, as confirmed by the low error of the linear calibration curve, showing a slope

of $2.66 \pm 0.01$ aC/ADC-channel and an offset referred to the input of $16.30 \pm 0.01$ aC.

## 2.4. Measurement setup with 4.5 MeV protons

To study the detectors by IBIC analysis, the proton micro-beam facility at the Ruđer Bošković Institute in Zagreb [25] was used. The system is based on a 6 MV Van-de-Graaff tandem accelerator. For the present work, protons were accelerated to gain an energy of 4.5 MeV, producing a micro-beam with a focus smaller than 2 µm (FWHM). At such an energy, a proton is stopped within 97 µm in diamond [26], so that they are completely absorbed within the detector volume. The spatial distribution of the ionization charge was evaluated by using SRIM, a software used to simulate ion transport in matter. For the IBIC measurements, the read-out chain consisted of a charge-sensitive preamplifier (ORTEC 142A) followed by a shaping amplifier (ORTEC 570) with a shaping time of 2 µs. Measurements were carried out by reducing connections to three adjacent strips, the central one for biasing and signal acquisition and the other two for grounding. A bias voltage in the ±300 V range was applied to the detector. A dedicated beam scanning and data acquisition system rasterized the beam in 128×128 pixels and read the amplitude of the charge signal with a trigger threshold regulated to 20.000 electrons, whereas for back-side irradiation it was lowered to about 10.000 electrons, because of a lower collection efficiency (protons are indeed completely stopped within the "dead" volume of the detector in this case). The read-out chain was calibrated with a silicon detector by assuming an electron-hole pair production energy of 3.62 eV [27]. Conversely, the CCE in diamond was determined by assuming an electron-hole pair production energy of 13.0 eV [28].

## 3. Results and discussion

### 3.1. Dark current measurements

The current-voltage (*I–V*) curves reported in fig. 3 were measured in the dark and at room temperature conditions with a Keithley 6517A pico-ammeter. Before the measurements, the device was heated at 100 °C in air for two minutes to remove any possible surface-adsorbed humidity able to modify the conductance value.

The *I–V* characteristic is fairly symmetric, and a linear behaviour is found up to 100 V. In such a range, the probed resistance of the detecting volume corresponds to about $1.6 \times 10^{14}$ Ω, addressing the low density of trap-and-release defects in the selected specimen.
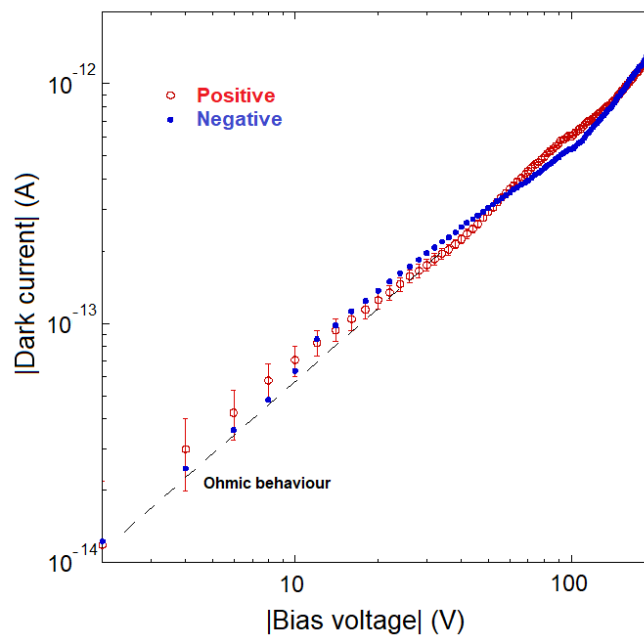
**Fig. 3**. Current-voltage characteristics of the fabricated device for both positive and negative bias voltages.

## 3.2. Electric field distribution: numerical analysis

Numerical simulations of the electric field distribution were carried out by using FlexPDE 5.0.4, a finite element software, on a 3D structure reproducing the real fabricated device with proper material conductivity, dielectric permittivity, and simulating the presence of both the graphite strips on the surface and the pillars embedded in the bulk diamond. For the analysis, diamond resistivity was set to $2 \times 10^{13}$ $\Omega$ cm, as inferred from dark current measurements reported in fig. 3. Resistivity of the surface graphite strips was set to $5 \times 10^{-5}$ $\Omega$ cm, on the basis of four-point probe measurements. Resistivity of the graphite pillars was set to $6.3 \pm 0.5$ $\Omega$ cm, as estimated by current-voltage measurements performed on "pass-through" columns fabricated by our group in other scCVD-diamond samples with the same laser treatment parameters used in the present work. Dielectric permittivity was set to 5.5 and 100 for diamond and graphite, respectively.

As reported in the simulation illustrated in fig. 4a, each $x$–$y$ 'elementary cell' exhibits wide regions of a weaker electric field far away from the pillars, whereas the density of the electric field lines increases in regions close to the pillars, which are highly defected regions as expected for a laser-processed volume. Therefore, the non-linearity of $I$-$V$ characteristics reported in fig. 3, where current approaches a $V^2$ dependence for $V > 100$ V, can be tentatively attributed to space charge limited current (SCLC) conduction mechanism [29, 30] usually

observed in diamond [31]. SCLC conduction regime could indeed be triggered by the progressive filling of the high density of traps concentrated in the neighborhood of the graphite pillars. It's worth mentioning here that the simulation shown in fig. 4a refers to a section located 100 µm below the top surface (which is about the stopping range of the 4.5 MeV protons): therefore, we can suppose that the influence of the top graphite contacts is not strong enough to distort the electric field lines.

Fig. 4b shows the cross-sectional ($x$–$z$) view of the distribution of the electric field contour lines in a region between two pillars at different potential. The direction of the simulated cross-section is represented by the blue solid line in fig. 4a. As expected, the electric field intensity distribution clearly indicates that charge collection mainly occurs along the detector volume defined by the pillars' length. Conversely, the electric field in the region below the pillars' end appears to be too weak (< 0.1 V/µm at an operating bias voltage of 200 V) to ensure an efficient charge collection. This will be confirmed by the results obtained under beta irradiation from the back-side.
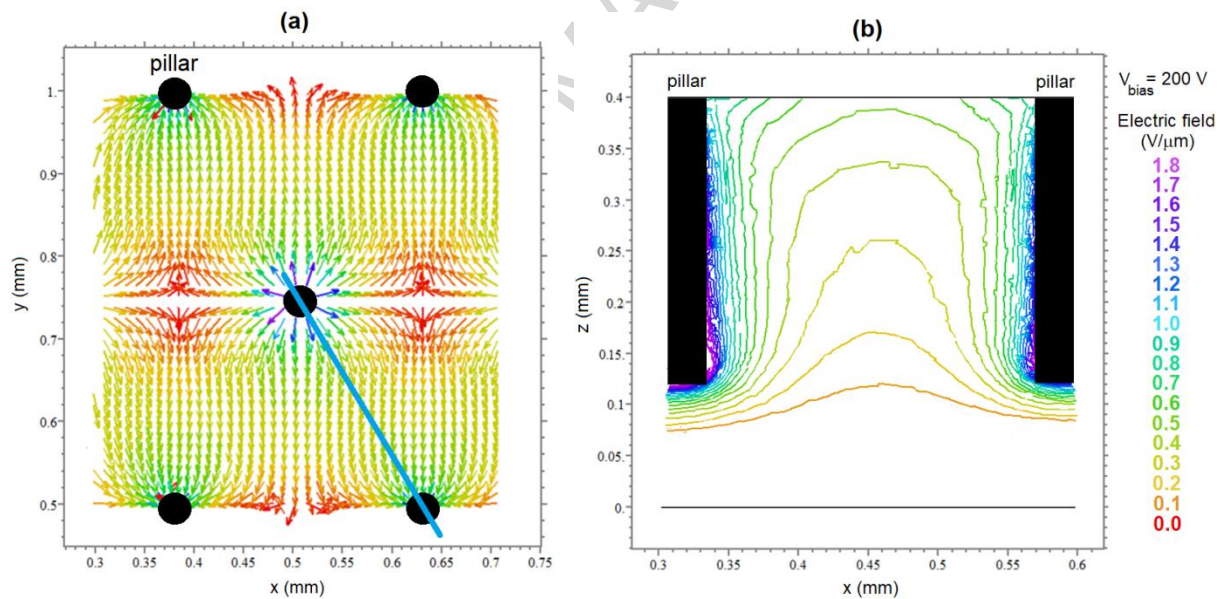


**Fig. 4**. Numerical simulations of the electric field distribution for the 3D detector at an operating bias voltage of 200 V. a) Electric field distribution in a zoomed region corresponding to an elementary $x$–$y$ rectangular cell, 100 µm below the top surface. Pillars located at $y = 0.5$ mm and $y = 1.0$ mm are at ground voltage, whereas the central one ($y = 0.75$ mm) is at bias potential. b) Cross-sectional view of the electric field contour lines distribution in the region between two pillars at different potential, positioned in the direction indicated by the blue solid line of fig. 4(a).

*3.3 Response to $^{90}$Sr electrons*

Fig. 5a shows the PHD of the collected charge at different positive bias voltages in the 100 – 200 V range for electrons impinging on the front surface of the detector (where graphitic strips were fabricated). Front-side irradiation allows the signal to be collected from both the lower energy electrons emitted in the $^{90}$Sr to $^{90}$Y decay, almost completely absorbed in the diamond detector volume, and the MeV range electrons emitted in the $^{90}$Y to $^{90}$Zr decay, traversing the whole device. Spectra were acquired without an external trigger (hampering in this way a correct estimation of the charge collection efficiency under beta particles), but using the self-triggering configuration of the internal digitizer. The threshold referred to the input was fixed to 0.24 fC (about 1500 electrons), being the amplitude of the Gaussian pedestal noise measured to be 0.18 fC (about 1100 electrons). Pulse distributions were monitored for 2700 s. As can be seen from fig. 5a, the typical asymmetric height distribution observed under *β*-source irradiation, with a long exponential decay tail, is observed. It's worth noting that, even at the lowest bias values, PHDs show a Most Probable Value (MPV) close to the one found at higher voltages (about 2 fC), denoting saturation of charge collection. Full Width Half Maximum (FWHM), which remains practically constant with bias voltage, is about $1.50 \pm 0.02$ fC: this large FWHM is mainly attributed to the contribution of the lower energy electrons emitted in the $^{90}$Sr to $^{90}$Y decay, which are almost fully absorbed within the diamond bulk.
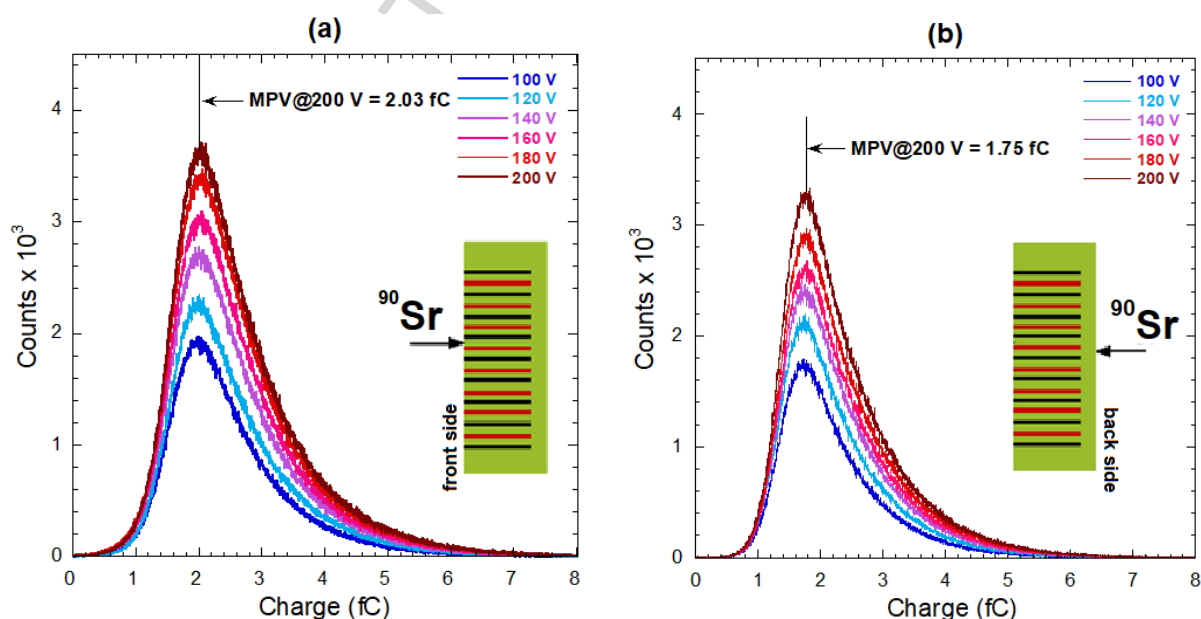


**Fig. 5**. PHDs at positive bias voltages in case of irradiation from the front side (a) and from the back side (b).

In order to confirm the effectiveness of pillars in collecting photogenerated charge, and to evaluate a signal contribution mainly induced by MeV range electrons, we performed measurements under $\beta$-particles impinging on the detector back side. In this configuration, most of the lower energy electrons emitted in the $^{90}$Sr to $^{90}$Y decay, as well as the 4.5 MeV protons (see section 3.4), are indeed absorbed in the 100 µm thick region below the pillars' end, where the electric field is less intense (see fig. 4b). Conversely, MeV range electrons are able to cross all the sample thickness, and to generate carriers also in regions where the electric field intensity is higher. Fig. 5b shows PHD results obtained at different positive applied voltages in the back-side configuration. As expected, both the MPV (about 1.75 fC) and the FWHM (about 1.30 fC) of the spectra are lower than the values obtained for the front-side measurements (fig. 5a), due to a decrease of the signal contribution coming from the lower energy electrons. Similar measurements, for both the front-side and back-side configurations, were performed by applying a negative bias: spectra showed approximately the same shape of the ones recorded at positive bias, with only slight differences ($< 5\%$) in terms of MPV and integral counts.
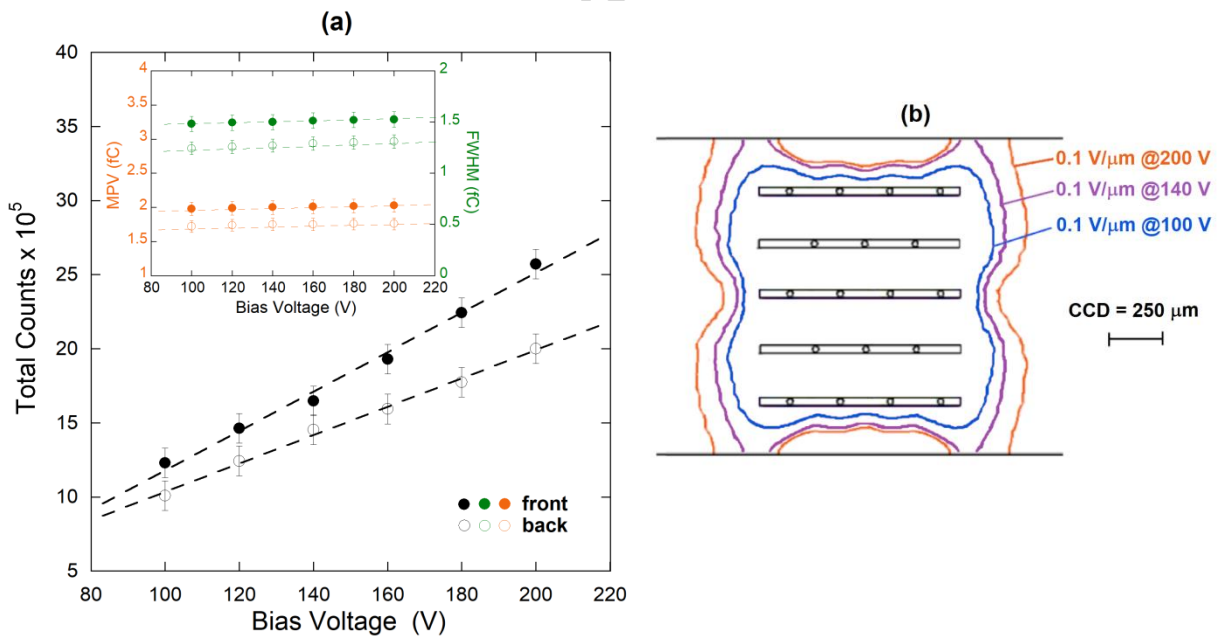


**Fig. 6**. a) Integral number of measured events at different positive bias voltages for $\beta$-particles impinging on the front (dots) and back (circles) side of the detector. In the inset, the sum of the MPV of collected charge and the FWHM of the distribution at different positive bias voltages for both the measurement configurations. b) Numerical simulation of the contour lines of a 0.1 V/µm electric field at three different bias voltages (100, 140 and 200 V). Without loss of generality, simulation was limited to a restricted number of strips and pillars, by taking into account, as a geometrical constraint, only the distance of the outer strips from the sample edge.

Fig. 6 reports the integral number of measured events (area under the curve of the beta spectrum) as a function of bias voltage for the two measurement configurations. Note that in both cases the total counts increase linearly with the applied bias, almost doubling their value from 100 to 200 V. The pulse pile-up at lower voltages and its rejection by the digitizer setup can only partially explain this dependence. The increase of counts cannot even be explained by a higher probability of collecting carriers (i.e. a better CCE); as can be indeed seen from the inset on fig. 6, both the MPV of collected charge and the FWHM of the distribution remain practically constant with applied voltage for both the front-side and back-side configurations, implying no significant shape changes in the beta spectrum, and therefore highlighting a good CCE in the span of bias used. Most probably, the increase of counts with voltage is due to an increase of the effective volume of the detector. It's worth recalling here that strips are only 1.5 mm long, whereas the sample lateral dimensions are $4 \times 4$ mm$^2$: being the whole volume of the detector irradiated by the $^{90}$Sr $\beta$-source, as described in section 2.3, it's plausible that a significant number of events occurring outside the volume defined by the surface strips and the graphite pillars are not counted, unless the charge carriers are generated within a distance from the electrodes equal to the charge collection distance (CCD), which can be expressed by CCD = $\mu\tau F$ where $\mu\tau$ is the mobility-lifetime product of charge carriers and $F$ is the applied electric field. The product $\mu\tau$ was previously evaluated to be about $2.5 \times 10^{-5}$ cm$^2$/V by independent X-ray photocurrent measurements [33] performed on a sample of the same quality as the one used in the present work. By considering an applied electric field $F = 0.1$ V/μm, chosen as a threshold value for an efficient charge collection, the corresponding CCD is 250 μm. As can be seen from fig. 6b, reporting a numerical simulation of the contour lines of a 0.1 V/μm electric field at three different bias voltages (100, 140 and 200 V), the increase of counts with voltage can be qualitatively explained by supposing an increasing number of events occurring within the evaluated CCD, actually expanding the collecting volume of the detector. In addition, de-trapping effects induced by the electric field, possibly enhanced by the radiation [34], may partially compensate for the recombination of charge carriers at defects, which are mostly concentrated in the neighborhood of pillars; this is also suggested by numerical simulations (fig. 4a), showing that the electric field in the regions surrounding pillars is particularly intense. The presence of electrically active carrier-selective defects (*i.e.* acting as traps for holes or for electrons) could also explain the slight difference for both the MPV and integral counts found at positive and negative applied voltages. Most likely, a class of defects which could act in our case as carrier traps is represented by N-V (nitrogen-vacancy) centers: a recent study [35] showed indeed that N-V photoluminescence is

greatly enhanced after the formation of laser-induced microstructures similar to those introduced in this work. By the way, a more detailed investigation is needed to figure out the effective nature of defects and the electronic processes involved in the observed behaviour.

It's worth observing now that back-side measurements allowed us to check qualitatively that pillars contribute to charge collection in conjunction with the surface graphite contacts. The average energy of the electrons emitted in the $^{90}$Sr to $^{90}$Y decay is 196 keV [36]: as can be seen from fig. 7, reporting a simulation of the energy distribution of 196 keV electrons as a function of penetration depth in diamond bulk, all the energy is deposited within a distance of only 120 µm.
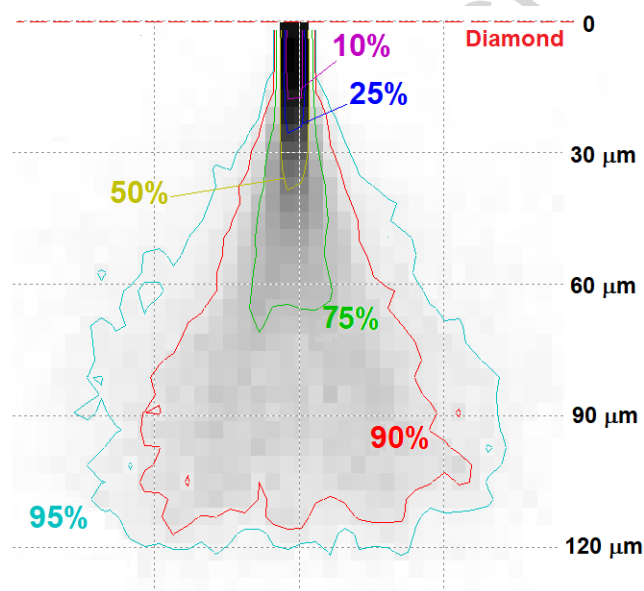


**Fig. 7**. Energy distribution of 196 keV electrons vs. penetration depth in diamond. Contour lines show the percentage of energy contained within the line. Simulation was performed with CASINO software [37].

As regards $^{90}$Y to $^{90}$Zr decay, the average energy of the electrons emitted is 926 keV [36]. Fig. 8 reports a simulation (a) of the energy distribution of 926 keV electrons as a function of penetration depth in diamond bulk, as well as a simulation (b) of the electric field contour lines in the region between two active pillars at different potential. Fig. 8c is similar to fig. 8b, but assumes that pillars are not working, and that the only active electrodes are the surface graphite strips. Note from fig. 8c that the 0.1 V/µm contour line is about 300 µm far away from the back surface (up in the figure): therefore, it's plausible that electrons emitted in the $^{90}$Sr to $^{90}$Y decay do not produce signal at all in case of inactive pillars. Conversely, active pillars (fig. 8b) are able to collect about the 25% of the deposited average energy, which is absorbed between 70 and 120 µm (see fig. 7) away from the back surface. On the other hand,

electrons emitted in the $^{90}$Y to $^{90}$Zr decay are on average able to produce charge collectable by the surface strips; however, a significant fraction (between 25 and 50%) of the deposited energy (*i.e.* absorbed in the first 300 μm of material) does not generate signal, whereas in case of working pillars this "lost" fraction is far less than 10% (see dashed lines in fig. 8).
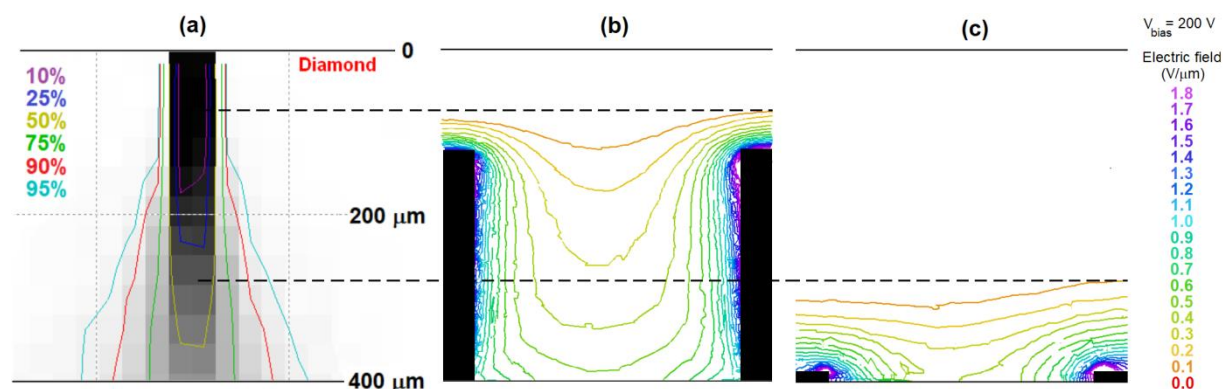


**Fig. 8**. Energy distribution of 926 keV electrons vs. penetration depth in diamond (a). Cross-sectional view of the electric field contour lines in the region between two active pillars at different potential (b). Cross-sectional view of the electric field contour lines in the region between two surface graphite contacts at different potential (c). Dashed lines are a guide to the eye to show the percentage of deposited energy able to generate signal in the two configurations of active electrodes (b) and (c).

Now, the MPV value of collected charge in case of back-side irradiation is only 14% less than the value obtained for front-side irradiation; this is inconsistent with the hypothesis that pillars are not working, since the difference between the amount of charge collected in the two configurations would have been, on the basis of the performed simulations (figs. 7 and 8), far larger than 14%, being surface strips unable to collect the charge produced by low-energy electrons and a significant fraction of the charge produced by MeV range electrons. Of course, a more complex analysis, based on finer simulation models of the energy spectrum of *β*-particles and of the collection efficiency of the detector, is needed to better understand and interpret quantitatively the experimental results.

### 3.4 IBIC results

Experiments with a 4.5 MeV proton beam were carried out at positive and negative bias voltages both in front-side and back-side configurations, in order to confirm the suitability of the particle detector to collect the charge carriers produced by the energy delivered within the sensing volume, as well as to confirm the performance estimated under *β*-particles irradiation. Proton mapping also allowed us to estimate the charge collection efficiency of the detector as

a function of the beam position, with a spatial resolution of a few micrometers.
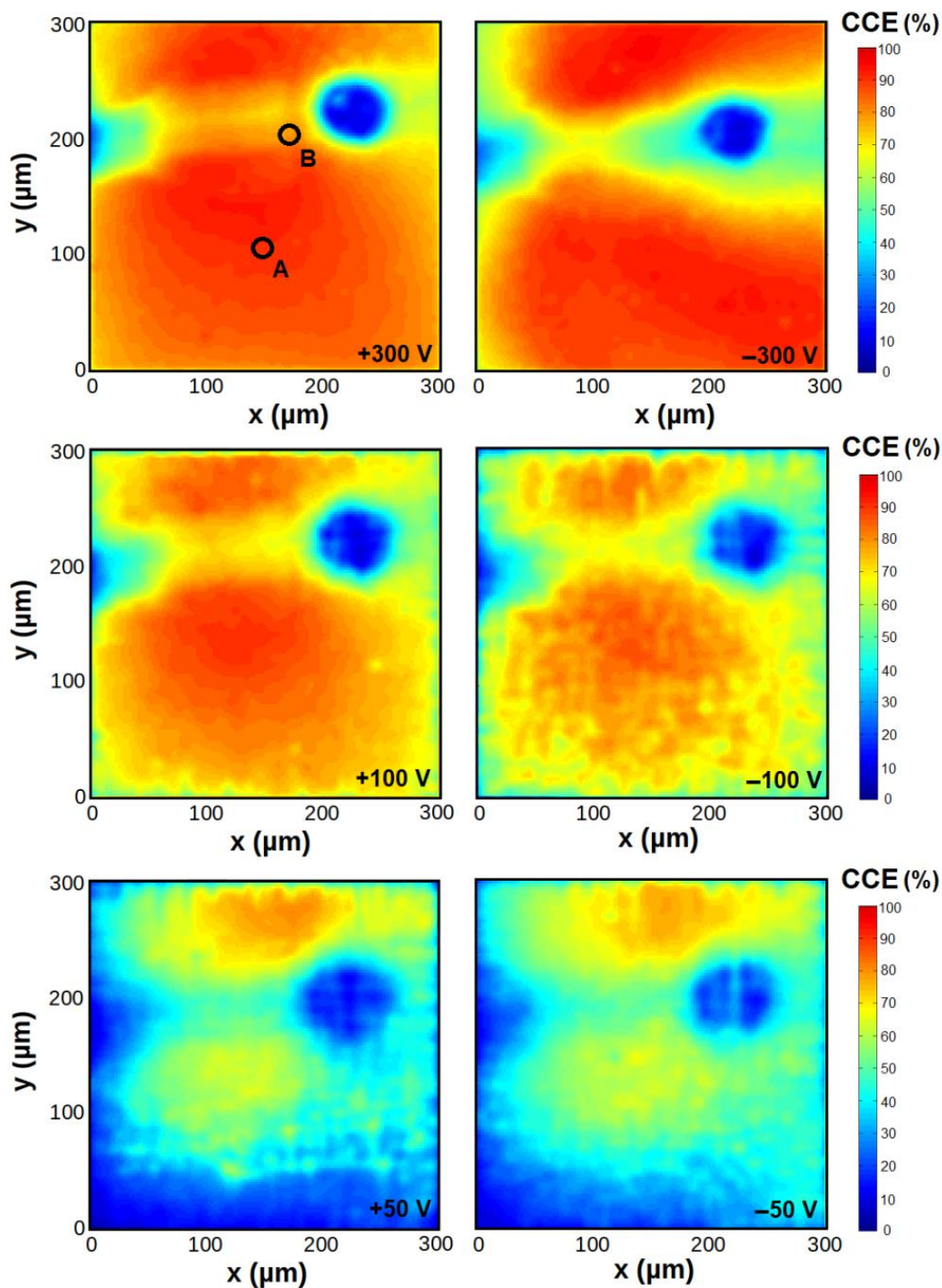


**Fig. 9**. IBIC signal response to proton micro-beam in case of front-side irradiation as a function of the beam position at different bias voltages: ± 300 V, ± 100 V, and ± 50 V. Empty dots marked with "A" and "B" indicate the points used for the estimation of the CCE curves reported in fig. 11.

Fig. 9 show the maps of the monitored signal for front-side irradiation on a $310 \times 310$ $\mu m^2$ area for three different positive (+300 V, +100 V, + 50 V) and negative (−300 V, −100 V, −50

V) bias voltages. Fig. 10 reports a sketch of the investigated regions in case of front-side and back-side irradiation.
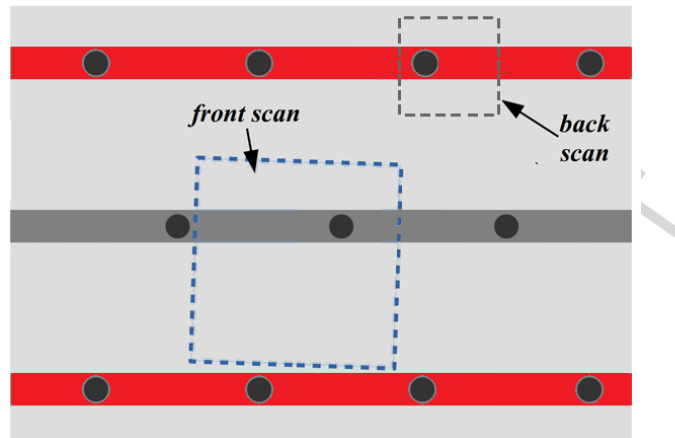


**Fig. 10** A sketch of the investigated regions under proton irradiation. Scanned areas are $310\times310$ μm$^2$ in the front-side configuration and $140\times140$ μm$^2$ in the back-side one, the results of which are shown in fig. 12.

As can be seen from fig. 9, as expected, CCE is extremely low (< 10%) in the area corresponding to the conducting pillar, approximately 30 μm in diameter, at every bias voltage applied. Conversely, charges are efficiently collected far away enough from the pillars. In particular, a better performance is obtained in the wide region between two differently polarized rows of pillars, whereas a lower CCE is obviously observed in the region between the pillars connected by the same surface graphite strip ($y = 200$ μm), *i.e.* at the same potential. As regards the absolute values of CCE, it is higher than 90% almost everywhere outside the pillars for $V = \pm 300$ V, it stays in the range 70 – 90 % for $V = \pm 100$ V, whereas it drops below 70% for $V = \pm 50$ V, even if there are rather wide regions (see the upper section of the maps) where CCE still reaches 80%. Interestingly, by comparing the cross-polarized image of fig. 2a and the proton maps of fig. 9, CCE seems not to be influenced by the amount of stress introduced within the diamond bulk: a good CCE is indeed observed also in the highly stressed regions between two rows of differently polarized pillars (white diagonal "plumes" in fig. 2a).
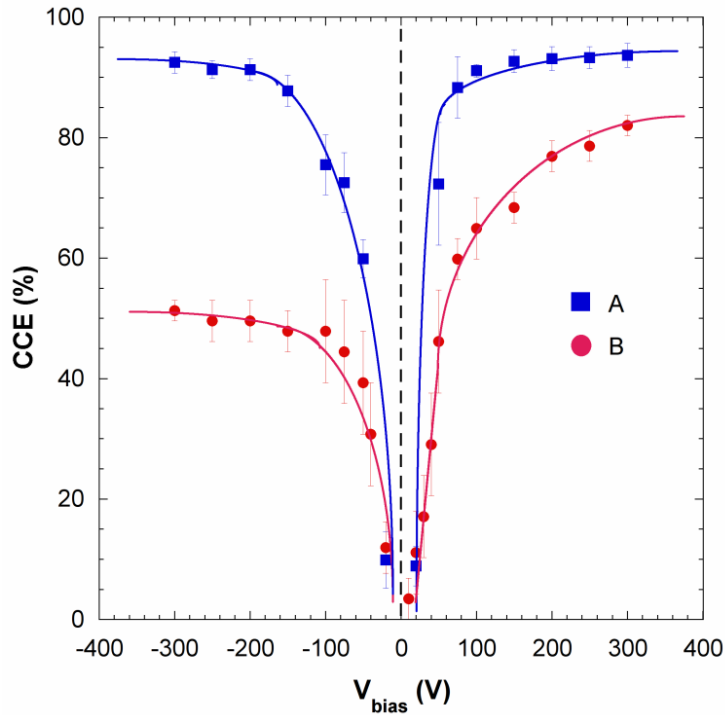
**Fig. 11**. Average charge collection efficiency (CCE) as a function of the applied bias voltage as measured with proton micro-beam in two different positions, as indicated in fig. 9 : "A" (far away from the pillar) and "B "(in the neighborhood of the pillar).

The rather high dependence of CCE on the polarity of bias voltage, observed in the neighborhood of the pillars, deserves further discussion. For this reason, CCE as a function of bias voltage was estimated in two different positions, indicated in fig. 9 (+300 V map) with "A" and "B". Results are reported in fig. 11. CCE increases in both cases with increasing bias voltage, due to a more intense electric field able to drift the generated carriers towards the buried contacts, finally saturating at high voltages. But CCE saturation values are completely different in the two cases, as well as its symmetry with polarity. As can be seen, in regions far away from the pillar (A), where the concentration of lattice defects is very low, CCE is fairly symmetric with polarity, and the saturation value (94%) is the same both in the positive and the negative branch. Conversely, in the neighborhood of the pillar (B), CCE saturation values are lower and a strong asymmetry with polarity is observed (CCE is up to 82% for positive bias and up to 52% for negative bias). The asymmetry with polarity observed in the B case seems to confirm the presence of electrically-active carrier-selective defects near the pillars which can trap one type of carriers, and from which de-trapping may occur or not depending on the polarity of the applied voltage. Unfortunately, IBIC alone is not a technique able to disentangle the contributions of electrons and holes to the collected charge signal, so to identify the polarity of traps. Possible and effective solutions to be adopted in the future

experiments are: 1) the implementation of IBIC, TRIBIC and TSC (Thermally Stimulated Current) analyses in the same experimental set-up [38]; 2) the analysis of ion beam-induced transient currents [39]. Finally, it's worth observing that maps recorded at ± 50 V are fairly symmetric with polarity, even in the neighborhood of the pillar, further indicating that pillars contribute to charge collection in conjunction with the surface graphite contacts.
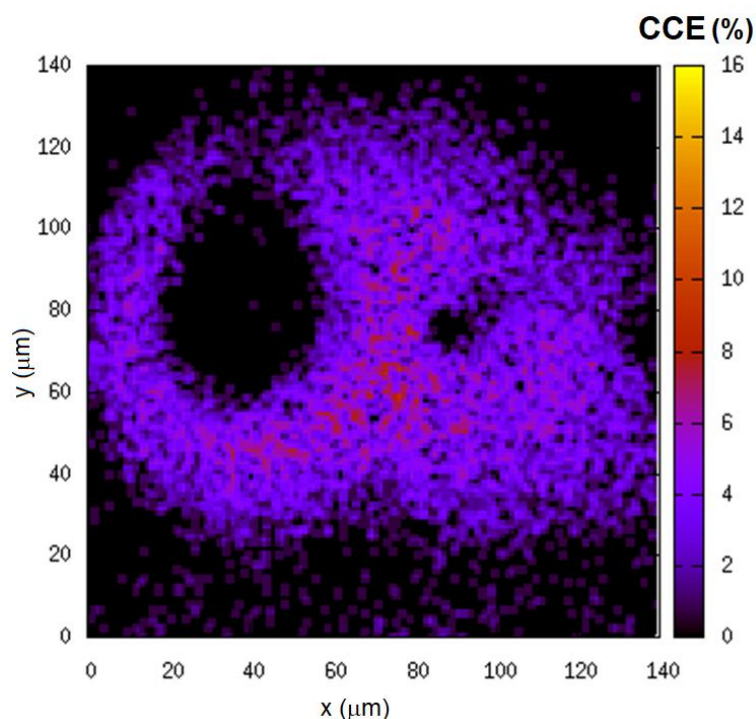


**Fig. 12**. Signal response under proton micro-beam irradiation on the back-side of the detector as a function of the beam position. The bias voltage is −300 V.

Fig. 12 reports the proton map of a 140×140 μm$^2$ region (see sketch in fig. 10) just around the pillar termination in case of back-side irradiation. As can be seen, unlike the case of front-side irradiation, charge collection efficiency is poor in this region of the detector, hardly reaching 10% and rapidly dropping below 2.8% (corresponding to the detection threshold of 10000 electrons) in the area corresponding to the pillar and few tens of μm away from it. The detectable signal (purple region) can be attributed to the electric field around the end of the pillar, intense enough (see simulation in fig. 4b) to partially collect charge despite the high density of defects in the neighborhood of the pillar and at the diamond/graphite interface. However, fig. 12 clearly indicates that the investigated pillar does not work properly. This is quite unexpected, because 4.5 MeV protons are stopped within 97 μm in diamond, so the majority of charge (Bragg peak) is deposited just where the end section of the pillar is located; a CCE < 10% is therefore not plausible with the assumption that the irradiated pillar

contributes to the signal. Presumably, that particular pillar is too defective, or, more probably, its resistivity is so high that the RC constant is much larger than the 2 µs shaping time of the read-out chain.

## 4. Conclusions

A single-crystal CVD diamond detector with 3D graphite pillars acting as buried contacts interconnected via surface graphite strips, both fabricated by femtosecond laser treatment, demonstrated its feasibility as an all-carbon device for particle detection, opening new perspectives for the realization of even more complex 3D architectures, such as 3D stacked detectors for particle tracking. Although cross-polarized optical microscopy and Raman analysis highlighted the presence of compressively stressed regions within the diamond bulk, good detection performance resulted from measurements under both beta particles and protons. An average charge collection efficiency of 94 % was measured under proton beam irradiation from the top surface. Numerical simulations of the electric field distribution showed that, despite the defects created in the regions surrounding the pillars, the electric field strength is high enough to partially compensate for the recombination of photogenerated carriers at electrically active carrier-selective defects. Further investigation is necessary to get a deeper insight into the electronic transport processes involved in the stressed/defected regions unavoidably created by the laser treatment used for the fabrication of 3D pillars.

## References

[1] F. Bachmair, Diamond sensors for future high energy experiments, *Nucl. Instr. Meth. Phys. Res. A*, 831 (2016) 370 – 377.

[2] M. Girolami, L. Criante, F. Di Fonzo, S. Lo Turco, A. Mezzetti, A. Notargiacomo, M. Pea, A. Bellucci, P. Calvani, V. Valentini and D.M. Trucchi, Graphite distributed

electrodes for diamond-based photon-enhanced thermionic emission solar cells, *Carbon*, 111 (2017) 48 – 53.

[3]   G. Pellegrini, P. Roy, A. Al-Ajili, R. Bates, L. Haddad, M. Horn, K. Mathieson, J. Melone, V. O'Shea, K.M. Smith, I. Thayne and M. Rahman, Technology development of 3D detectors for medical imaging, *Nucl. Instr. Meth. Phys. Res. A* 504 (2003) 149 – 153.

[4]   R. Battiston, The MEMS Poject, in Astroparticle, Particle and Space Physics, Detectors and Medical Physics Applications, *Proceedings of the 10th Conference*, World Scientific Publishing Co. Re. Ltd., M. Barone, A. Gaddi, C. Leroy, L. Price, P.G. Rancoita, R. Rucht, Eds., 2008.

[5]   S.I. Parker, C.J. Kenney and J. Segal, 3D - A proposed new architecture for solid-state radiation detectors, *Nucl. Instr. Meth. Phys. Res. A* 395 (1997) 328 – 343.

[6]   A. Oh, B. Caylar, M. Pomorski and T. Wengler, A novel detector with graphitic electrodes in CVD diamond, *Diamond Relat. Mater.,* 38 (2013) 9 – 13.

[7]   S. Lagomarsino, M. Bellini, C. Corsi, F. Gorelli, G. Parrini, M. Santoro and S. Sciortino, Three-dimensional diamond detectors: Charge collection efficiency of graphitic electrodes, *Appl. Phys. Lett.,* 103 (2013) 233507.

[8]   T. Kononenko, V. Ralchenko, A. Bolshakov, V. Konov, P. Allegrini, M. Pacilli, G. Conte and E. Spiriti, All-carbon detector with buried graphite pillars in CVD diamond, *Appl. Phys. A Mater. Sci Proc.* 114 (2014) 297 – 300.

[9]   R. Walker, S. Prawer, D.N. Jamieson, K.W. Nugent and R. Kalish, Formation of buried p-type conducting layers in diamond, *Appl. Phys. Lett.,* 71 (1997) 1492 – 1494.

[10]  T.V. Kononenko, M. Meier, M.S. Komlenok, S.M. Pimenov, V. Romano, V.P. Pashinin and V.I. Konov, Microstructuring of diamond bulk by IR femtosecond laser pulses, *Appl. Phys. A Mater. Sci Proc.* 90 (2008) 645 – 651.

[11]  T.V. Kononenko, A.A. Khomich and V.I. Konov, Peculiarities of laser-induced material transformation inside diamond bulk, *Diamond Relat. Mater.,* 37 (2013) 50 – 54.

[12]  S. Lagomarsino, M. Bellini, C. Corsi, F. Gorelli, G. Parrini, M. Santoro and S. Sciortino, Three-dimensional diamond detectors: Charge collection efficiency of graphitic electrodes, *Appl. Phys. Lett.,* 103 (2013) 233507.

[13]  S. Lagomarsino, S. Sciortino, B. Obreshkov, T. Apostolova, C. Corsi, M. Bellini, E. Berdermann and C.J. Schmidt, Photoionization of monocrystalline CVD diamond irradiated with ultrashort intense laser pulse, *Phys. Rev. B* 93 (2016) 085128.

[14]  G. Conte, P. Allegrini, M. Pacilli, S. Salvatori, T. Kononenko, A. Bolshakov, V. Ralchenko and V. Konov, Three-dimensional graphite electrodes in CVD single crystal diamond detectors: Charge collection dependence on impinging *β*-particles geometry, *Nucl. Instrum. Meth. Phys.Res. A* 799 (2015) 10 – 16.

[15]  B. Sun, P. S. Salter, M. J. Booth, High conductivity micro-wires in diamond following arbitrary paths, *Appl. Phys. Lett.*, 105 (2014) 231105.

[16]   M. Girolami, A. Bellucci, P. Calvani, S. Orlando, V. Valentini and D. M. Trucchi, Raman investigation of femtosecond laser-induced graphitic columns in single-crystal diamond, *Appl. Phys. A Mater. Sci. Proc.* 117 (2014) 143 – 147.

[17]  D. Asner et al., Diamond pixel modules, *Nucl. Instr. Meth. Phys. Res. A* 636 (2011) S125–S129.

[18]  G.T. Forcolin, V. Grilj, B. Hamilton, L. Li, M. McGowan, S.A. Murphy, A. Oh, N. Skukan, D. Whitehead and A. Zadoroshnyj, Study of a 3D diamond detector with photon and proton micro-beams, *Diamond Relat. Mater.,* 65 (2016) 75–82.

[19]  M.J. Booth, G.T. Forcolin, V. Grilj, B. Hamilton, I. Haughton, M. McGowan, S.A. Murphy, A. Oh, P.S. Salter, I. Sudić and N. Skukan, Study of cubic and hexagonal cell geometries of a 3D diamond detector with a proton micro-beam, *Diamond Relat. Mater.,* 77 (2017) 137 – 145.

[20]  S. Murphy, M. Booth, L. Li, A. Oh, P. Salter, B. Sun, D. Whitehead and A. Zadoroshnyj, Laser processing in 3D diamond detectors, *Nucl. Instr. Meth. Phys. Res. A* 845 (2017) 136 – 138.

[21]  http://e6cvd.com/media/wysiwyg/pdf/E6_CVD_Diamond_Handbook_A5_v10X.pdf

[22]  M. Pacilli, P. Allegrini, M. Girolami, G. Conte, E. Spiriti, V. G. Ralchenko, M. S. Komlenok,  A. A. Khomic and V. I. Konov, Polycrystalline CVD diamond pixel array detector for nuclear particles monitoring, *Journal of  Instrumentation,* 8 (2013) C02043.

[23]  M. Komlenok, A. Bolshakov, V. Ralchenko, V. Konov, G. Conte, M. Girolami, P. Oliva and S. Salvatori, Diamond detectors with laser induced surface graphite electrodes, *Nucl. Instr. Meth. Phys. Res. A*, 837 (2016) 136–142.

[24] A. Tardieu, F. Cansell, J. P. Petitet, Pressure and temperature dependence of the first-order Raman mode of diamond, *J. Appl. Phys,* 68 (1990) 3243–3245.

[25] M. Jakšić, I. Bogdanović Radović, M. Bogovac, V. Desnica, S. Fazinić, M. Karlušić, Z. Medunić, H. Muto, Z. Pastuović, Z. Siketić, N. Skukan and T. Tadić, New capabilities of the Zagreb ion micro-beam system, *Nucl. Instr. Meth. Phys. Res. B* 260 (2007) 114-118.

[26] J. F. Ziegler, M.D. Ziegler and J. P. Biersack, SRIM-2012.03, Stopping and Range of Ions in Matter, 2013.

[27] G. F. Knoll, Radiation Detection and Measurements, 3rd ed. (John Wiley & Sons, 2000).

[28] L. S. Pan, S. Han, and D. R. Kania, Diamond: Electronic Properties and Applications (Kluwer Academic, Dordrecht, 1995).

[29] M. A. Lumpert, Simplified Theory of Space-Charge-Limited-Currents in an Insulator with Traps, *Phys. Rev*., 103 (1956) 1648-1656.

[30] F.C. Chiu, A Review on Conduction Mechanisms in Dielectric Films, *Advances in Materials Science and Engineering*, 2014, 578168.

[31] G. Conte, M. Girolami, S. Salvatori and V. Ralchenko, X-ray diamond detectors with energy resolution, *Appl. Phys. Lett.,* 91 (2007) 183515.

[32] D. R. Kania, M. I. Landstrass, M. A. Plano, L. S. Pan, and S. Han, Diamond radiation detectors, *Diamond Relat. Mater.*, 2 (1993) 1012 – 1019.

[33] D. M. Trucchi, P. Allegrini, P. Calvani, A. Galbiati, K. Oliver, and G. Conte, Very Fast and Primingless Single-Crystal-Diamond X-Ray Dosimeters, *IEEE Electron Device Lett*., 33 (2012) pp. 615-617.

[34] M. Girolami, A. Bellucci, P. Calvani, R. Flammini, and D. M. Trucchi, Radiation-assisted Frenkel-Poole transport in single-crystal diamond, *Appl. Phys. Lett.,* 103 (2013) 083502.

[35] S. M. Pimenov, B. Neuenschwander, B. Jäggi, and V. Romano, Effect of crystal orientation on picosecond-laser bulk microstructuring and Raman lasing in diamond,

*Appl. Phys. A Mater. Sci. Process.*, 114 (2014) 1309 – 1319.

[36] Table de Radionucléides, Note technique LNHB 2011/53, CEA, LIST, LNA-LNHB – France 2011.

[37] D. Drouin, A. Réal Couture, D. Joly, X. Tastet, V. Aimez, and R. Gauvin, CASINO V2.42 - A Fast and Easy-to-use Modeling Tool for Scanning Electron Microscopy and Microanalysis Users, *Scanning*, 29 (2007) 92 – 101.

[38] Z. Medunić, Ž. Pastuović, M. Jakšić, and N.Skukan, Studying of trap levels by the use of focused ion beams, *Nucl. Inst. Meth. Phys. Res. B*, 231 (2005) 486 – 490.

[39] N. Skukan, V. Grilj, and M. Jakšić, CVD diamond as a position sensitive detector using charge carrier transition time", *Nucl. Inst. Meth. Phys. Res. B*, 306 (2013) 186 – 190.

**Graphical abstract**
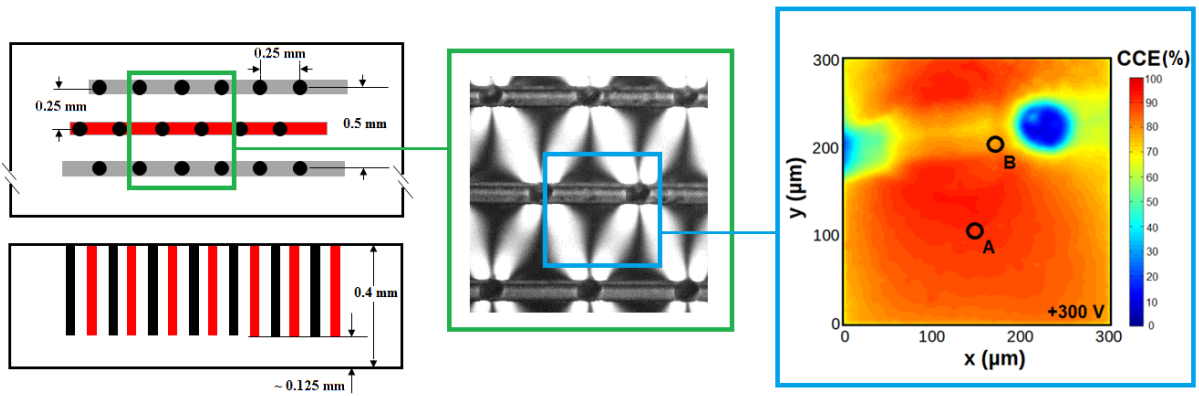
## Highlights

- All-carbon 3D diamond detectors with buried graphite pillars and surface graphite contacts were tested under $\beta$-particles and protons.

- Pillars are not "pass-through", enabling an easy implementation of 3D stacked diamond detectors for particle tracking.

- A comprehensive study including crossed-polarizers imaging, numerical simulation of the electric field lines in the detector volume, $\beta$-particle characterization, and proton mapping is reported.

- Charge collection efficiency ( $> 90\%$ ) is not affected by the stress induced by the fabrication of the pillars within the diamond bulk.